Nek5000 Users' Guide

1 Introduction

Nek5000 solves several partial differential equations related to incompressible fluid flow, thermal or species transport, and incompressible magnetohydrodynamics (MHD). This section gives a brief overview of the equations involved. Subsquent sections outline particular applications and results obtained with Nek5000. Input files for most of the cases are provided or described in the Appendix.

1.1 Incompressible Navier-Stokes Equations

The primary set of equations solved by Nek5000 are the incompressible Navier-Stokes equations (NSE)

$$
\begin{aligned}
\rho\left(\frac{\partial \mathbf{u}}{\partial t}+\mathbf{u}\cdot\nabla\mathbf{u}\right) &= -\nabla p + \nabla\cdot\mu\left(\nabla\mathbf{u}+(\nabla\mathbf{u})^T\right) + \mathbf{f}, && (1)\\
\nabla\cdot\mathbf{u} &= 0, && (2)
\end{aligned}
$$

in $\Omega \times [0, t_f]$ where $\mathbf{f}(\mathbf{x}, t)$ is a user-defined forcing function. These equations are solved simultaneously with the energy equation

$$
\begin{aligned}
\rho C_p\left(\frac{\partial T}{\partial t}+\mathbf{u}\cdot\nabla T\right) &= \nabla\cdot k\nabla T + q, && (3)\\
& && (4)
\end{aligned}
$$

with $q(\mathbf{x}, t)$ a user-defined volumetric heat source. Initial conditions in the domain $\Omega \subset \mathbb{R}^d$, d=2 or 3, and bounary conditions for $\mathbf{u}$ and T on $\partial\Omega$ are typically specified through fortran function calls in the `.usr` file.

For the majority of the flow cases (e.g., constant viscosity with no free surfaces) the equations are advanced without the second expression in the stress tensor, which is nominally zero because of the divergence-free constaint (2). One can nondimensionalize the equations by rescaling with respective characteristic length and time scales, L and U/L, where U is a velocity associated with the problem specification. Multiplying (1) by $\frac{L}{U^2}$ and (2) by $\frac{L}{U}$, one obtains the nondimensional form

$$
\begin{aligned}
\frac{\partial \mathbf{u}}{\partial t}+\mathbf{u}\cdot\nabla\mathbf{u} &= -\nabla p + \frac{1}{Re}\nabla^2\mathbf{u} + \mathbf{f}, && (5)\\
\nabla\cdot\mathbf{u} &= 0, && (6)
\end{aligned}
$$

where $Re := \rho UL/\mu$ is the Reynolds number, p and $\mathbf{f}$ have been scaled by ρ^{-1} and $\mathbf{u}$ by U^{-1}. Here, we've assumed constant viscosity μ and density ρ and have thus dropped the second term in the viscous stress tensor to arrive at the familiar so-called *Laplacian* formulation. When using Nek5000 with the full stress tensor, we refer to it as the *stress* formulation.

Nek5000 solves the NSE in dimensional form. It can be used in nondimensional form by setting $U = L = \rho \equiv 1$ and $\mu = Re^{-1}$. An advantage of the nondimensional form (based on convective velocity U) is that physical simulation times, tolerances, etc. tend to be easy to set based on prior experience with other simulations. Nek5000 will automatically choose iteration tolerances in the dimensional case, but they tend to be (perhaps overly) conservative. If warranted, one can tune the iteration tolerances for optimal performance.

1.2 Low Mach Number Formulation

Nek5000 also supports a low Mach number formulation, which can be used in the incompressible limit. The equations are

LOW MACH NUMBER EQUATIONS

Example Cases

This section provides a collection of Nek5000 examples illustrating basic approaches and results.

2 Kovasznay Solution

Kovasznay[1] gives an analytical solution to the steady-state Navier-Stokes equations that is similar to the two-dimensional flow-field behind a periodic array of cylinders (Fig. 1a),

$$\begin{aligned} u_x &= 1 - e^{\lambda x}\cos 2\pi y \\ u_y &= \tfrac{\lambda}{2\pi} e^{\lambda x}\sin 2\pi y \end{aligned} \qquad \lambda := \frac{Re}{2} - \sqrt{\frac{Re^2}{4} + 4\pi^2},$$

where Re is the Reynolds number based on mean flow velocity and separation between vortices.

We use E=8 elements in a mesh with periodic boundary conditions at $y = \frac{1}{2} \pm 1$ and Dirichlet conditions given by the exact solution at $x = -\frac{1}{2}$, 1. The solution is time marched to advect initial errors out the domain: $t_f = 8$ with Δt=.001, corresponding to CFL=.344 for N=16. For lower N, one could choose a larger timestep and still satisfy $CFL< 0.5$.[2] Nek5000 supports BDF/EXT and characteristics-based timestepping,[3] both of which are kth-order accurate. (Set TORDER=k, k=1–3, and IFCHAR to T or F in the .rea file.) The BDF/EXT scheme requires one nonlinear evaluation per step and has a stability limit of $CFL\sim .62$. The characteristics scheme allows $CFL\sim$ 2–4 but is more expensive per step and has an $O(\Delta t^k)$ error that persists at steady-state.

Exponential convergence is seen in Fig. 1b for both the $\mathbb{P}_N - \mathbb{P}_{N-2}$ and splitting methods with BDF/EXT. At lower N, splitting is more accurate because of its Nth-order pressure approximation. The residual steady-state error of the characteristics method exhibits the expected 8-fold error reduction as Δt is reduced to .0005.

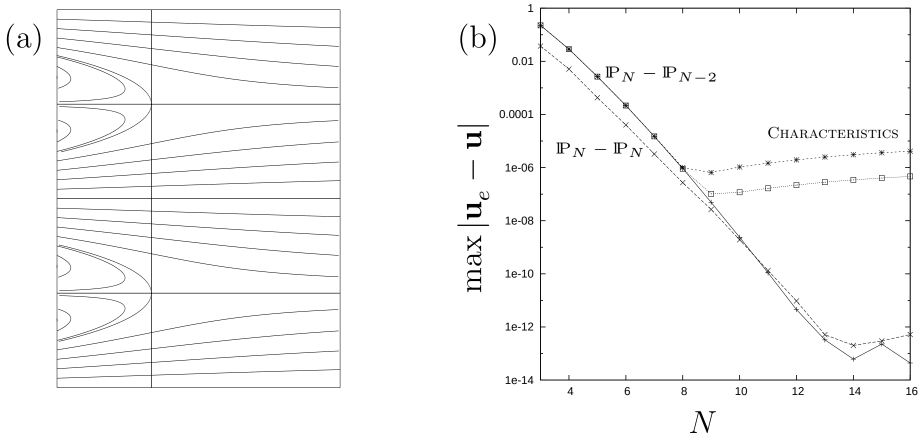

Figure 1: Kovasznay flow at $Re = 40$: (a) mesh and streamlines; (b) semilog plot of error vs polynomial N shows exponential convergence. Near machine precision is realized with BDF/EXT, whereas characteristics saturates with a residual steady-state error that is observed to be $O(\Delta t^3)$.

---

[1] L. Kovasznay, "Laminar flow behind a two-dimensional grid," *Proc. Cambr. Philos. Soc.* **44**, 58–62 (1948).

[2] See (3.5.13) in Deville, Fischer, and Mund, *High-Order Methods for Incompressible Flows*, 2002.

[3] Maday, Patera, and Rønquist, "Operator Integration-Factor Splitting Method for Time-Dependent Problems: Application to Incompressible Fluid Flow," *J. Sci. Comput.* **5** 263–292, 1990.

3 Rayleigh-Benard Convection

Chandrasekhar[4] has carefully studied linear stability of Rayleigh-Benard convection using the Boussinesq approximation, given in terms of the Rayleigh (Ra) and Prandtl (Pr) numbers as

$$\frac{\partial \mathbf{u}}{\partial t} + \mathbf{u}\cdot\nabla\mathbf{u} = -\nabla p + Pr\nabla^2\mathbf{u} - RaPrT, \qquad \frac{\partial T}{\partial t} + \mathbf{u}\cdot\nabla T = \nabla^2 T,$$

along with continuity, $\nabla\cdot\mathbf{u}$=0. Above a certain critical Rayleigh number Ra_c, the conduction due to adverse temperature gradient becomes linearly unstable to small perturbations and convection rolls develop (Fig. 2 top). The table below shows predictions of Ra_c at the most unstable wavenumber k_c for $\Omega = [0 : 2\pi/k_c] \times [0 : 1]$ having periodic conditions in x. Dirichlet conditions $T = 1 - y$ are specified for temperature on the horizontal boundaries, and three different conditions are considered for velocity: both walls (Dirichlet-Dirichlet), both stress-free (Neumann-Neumann) and a mix (Dirichlet-Neumann).

Critical Rayleigh number for 3 types of boundaries							
BC	Ra_{12}	Ra_{23}	Ra_c[4]	k_c[4]	Ra_1	Ra_2	Ra_3
D–D	1707.75	1707.74	1707.76	3.117	1760	1740	1725
D–N	1100.71	1100.64	1100.65	2.682	1144	1122	1111
N–N	657.639	657.566	657.511	2.2214	690	680	670

According to dynamical systems theory, the saturation amplitude (U) and kinetic energy ($\bar{E_k}$) grow, respectively, as $\sqrt{\epsilon}$ and ϵ, for $\epsilon := (Ra - Ra_c)/Ra_c \ll 1$. Thus Ra_c can be determined from a linear fit of (volume-averaged steady state) $\bar{E_k}$ versus Ra for two or more values of Ra as shown in Fig. 2 (left). In the table above, the estimates Ra_{12} and Ra_{23} are determined from solution pairs at (Ra_1, Ra_2) and (Ra_2, Ra_3), respectively. For each case, E_k is computed in a single unsteady run (Fig. 2 right) by varying Ra after time marching to a steady state such that $|dE_k/dt| \leq \sigma \times \bar{E_k}$ with $\sigma = 10^{-4}$. Larger σ or lower polynomial orders $N < 7$ lead to a drop in accuracy for the estimates of Ra_c. Iteration tolerances were controlled by setting TOLREL $= 10^{-5}$. Larger values (10^{-3}) did not yield a clear initial linear stage with exponential growth but the Ra_c estimate was not affected.

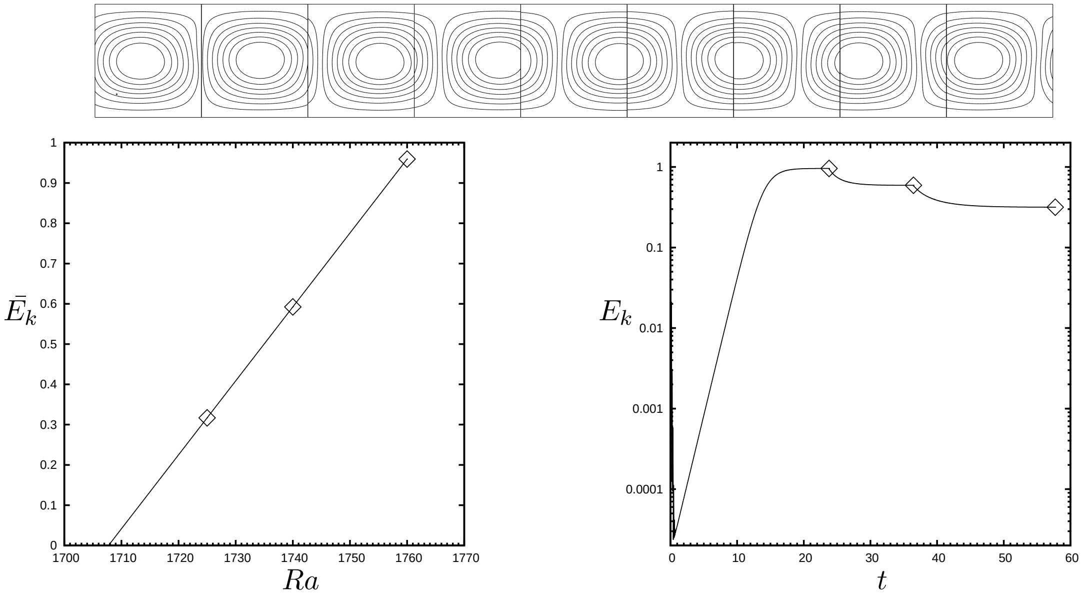

Figure 2: Rayleigh-Benard convection with walls: (top) streamlines for E=9 elements and N=7; (left) kinetic energy for E=3 and N=7 versus Rayleigh number and (right) time.

---

[4] S. Chandrasekhar, "Hydrodynamic and Hydromagnetic Stability," Oxford University Press (1961)

4 Convection in a 2D Annulus

This case demonstrates the application of Nek5000 to simulation of natural convection between the two concentric cylinders as considered by Grigull & Hauf [5] and presented by Van Dyke [6]. The inner cylinder (diameter D) is slightly heated with with respect to the outer one (diameter $3D$). The Boussinesq approximation is used to formulate the equations of motion, valid in situations where density differences are small enough to be neglected everywhere except in the gravitational forcing.

Normalizing the Navier-Stokes and energy equations with D for the length scale and D/U for the time scale ($U \sim \sqrt{\alpha\, g\, D\, (T_1 - T_0)}$ is the characteristic velocity in the given problem), and introducing nondimensional temperature $\theta = (T - T_0)/(T_1 - T_0)$, where T_0 and T_1 are the respective temperatures of the outer and inner cylinders, the governing equations take the nondimensional form

$$\begin{aligned} \frac{\partial \mathbf{u}}{\partial t} + \mathbf{u}\cdot\nabla\mathbf{u} &= -\nabla p + \frac{1}{\sqrt{Gr}}\nabla^2\mathbf{u} + \theta, \qquad \nabla\mathbf{u} = 0 \\ \frac{\partial \theta}{\partial t} + \mathbf{u}\cdot\nabla\theta &= \frac{1}{\sqrt{Gr}\, Pr}\theta. \end{aligned} \tag{7}$$

where two nondimensional parameters were introduced

$$Gr = \frac{\alpha\, g\, (T_1 - T_0)\, D^3}{\nu^2}, \qquad Pr = \frac{k}{\nu}, \tag{8}$$

denoting Grashof number and Prandtl number, respectively. Here, $\mathbf{u}$ is the velocity vector, p is the pressure divided by density, ν is the kinematic viscosity, α is the volumetric thermal expansion coefficient, and g is the acceleration due to gravity.

The computational mesh for a steady-state result at Gr=120,000 and $Pr = 0.8$ is shown in Fig. 3 (left). The simulations are run until the computational time $t\, D/U \sim 1000$, by which time a steady-state solution is obtained, indicated by the change in velocity magnitude $\sim 10^{-7}$ between successive time steps. The steady-state streamlines and isotherms are visualized in Fig. 3 center and right panels. The results are in excellent agreement with the results of Grigull & Hauf that were published by Van Dyke.

---

[5] Grigull & Hauf, Proc. of the 3rd Int. Heat Transfer Conf. 2, p. 182–195 (1966)

[6] M. Van Dyke *An Album of Fluid Motion*, Parabolic Press, Stanford, CA, 1982

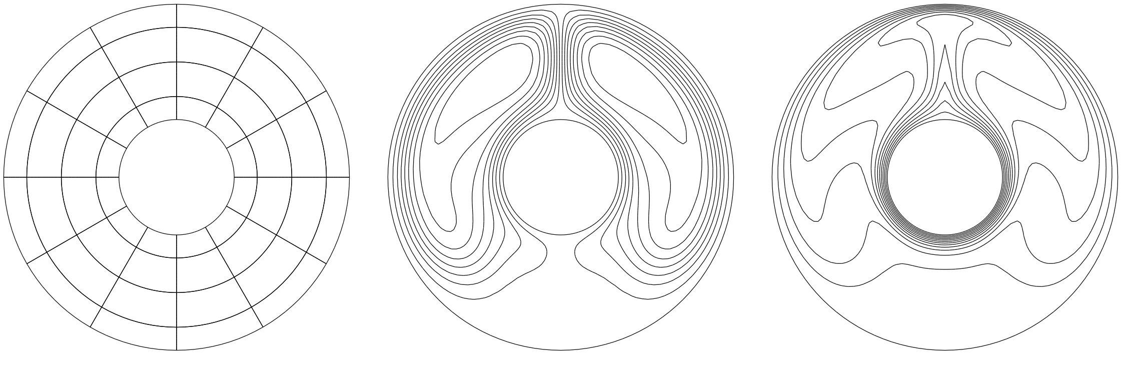

Figure 3: 2D natural convection: (left) mesh with E=32 spectral elements; (center) streamlines for Gr=120,000; and (right) isothermal lines.

5 Navier-Stokes Eigenfunctions

Walsh[7] derived a family of exact eigenfunctions for the Stokes and Navier-Stokes equations based on a generalization of Taylor-Green vortices in the periodic domain $\Omega = [0, 2\pi]^2$. For all integer pairs (m, n) satisfying $\lambda = -(m^2 + n^2)$, families of eigenfunctions can be formed by defining streamfunctions that are linear combinations of the functions

$$\cos(mx)\cos(ny),\ \sin(mx)\cos(ny),\ \cos(mx)\sin(ny),\ \sin(mx)\sin(ny).$$

Taking as an initial condition the eigenfunction $\mathbf{u}' := (-\psi_y, \psi_x)$, a solution to the Navier-Stokes equations is $\mathbf{u} = e^{\nu\lambda t}\mathbf{u}'(\mathbf{x})$. (Note that pressure precisely balances the $2m$ and $2n$ wavenumbers arising from the quadratic terms, as it must.) Figure 4 shows the vorticity for a case proposed by Walsh, with $\psi = (1/4)\cos(3x)\sin(4y) - (1/5)\cos(5y) - (1/5)\sin(5x)$. The solution is stable only for modest Reynolds numbers. Interesting long-time solutions can be realized, however, by adding a relatively high-speed mean flow $\mathbf{u}_0$, in which case the solution is $\mathbf{u}(\mathbf{x}, t) = \mathbf{u}_0 + e^{\nu\lambda t}\mathbf{u}'[\mathbf{x} - \mathbf{u}_0 t]$, where the brackets imply that the argument is modulo 2π in x and y. By varying $\mathbf{u}_0$, one can advect the solution a significant number of characteristic lengths before the eigensolution decays.

The right two panels in Fig. 4 show the spatial and temporal errors for the solution on the left with $\nu = .05$ and $\mathbf{u}_0 = (16, 5)$, for which a feature of characteristic length $l{=}2\pi/5$ is propagated $\approx 25l$ by final time $t{=}2$. The center panel shows that characteristics scheme yields expected kth-order accuracy when TORDER=k, $k{=}2$ or 3. The right panel shows that exponential convergence vs. N for both the $\mathbb{P}_N - \mathbb{P}_{N-2}$ and $\mathbb{P}_N - \mathbb{P}_N$ methods, with the latter having lower error. As N is increased, the error saturates to the temporal truncation error. For the characteristics scheme, the error for $\Delta t{=}.0001$ is $5.8{\times}10^{-8}$, while for extrapolation it is $1.4{\times}10^{-6}$. In contrast to the steady-state Kovasznay case, the characteristics scheme is more accurate than extrapolation.

Also shown in the right panel is the error for the $\mathbb{P}_N - \mathbb{P}_{N-2}$/characteristics combination when using a mesh comprising $E{=}E_1 \times E_1$ elements, with $E_1{=}4$ and 8. For the $E_1{=}4$ case, a final error of $< .01$ is realized with $N{=}7$, corresponding to 5.6 points/wavelength. For $E_1{=}8$, a final error of .0023 is attained with $N{=}5$, corresponding to 8 points per wavelength.

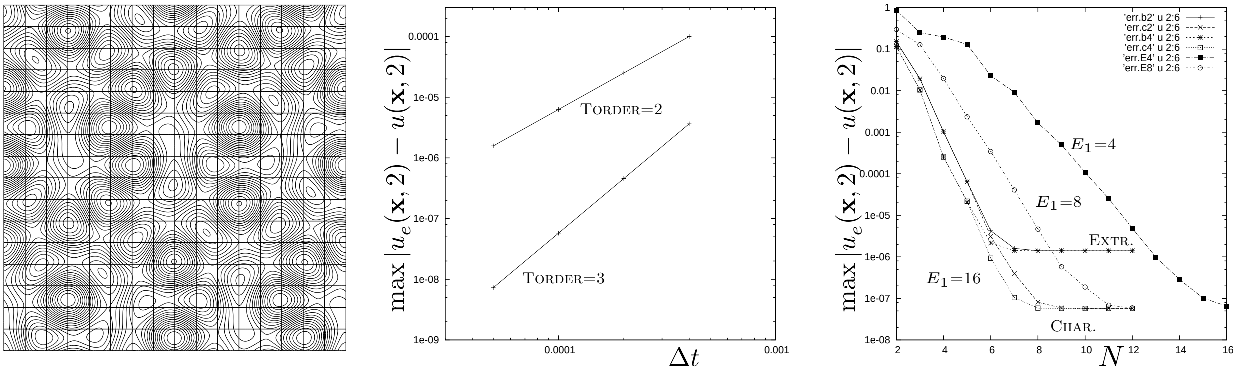

Figure 4: Eddy solution results: (left) vorticity at $t{=}2$ for $N{=}15$, (center) error vs Δt for $\mathbb{P}_N - \mathbb{P}_{N-2}$ with $N{=}15$ and IFCHAR=T, and (right) error vs polynomial order N for $\mathbb{P}_N - \mathbb{P}_{N-2}$ and $\mathbb{P}_N - \mathbb{P}_N$ with $\Delta t{=}.0001$ and IFCHAR=F/T (i.e., extrapolation or characteristics).

---

[7] O. Walsh, "Eddy solutions of the Navier-Stokes equations," *The NSE II-Theory and Numerical Methods*, J.G. Heywood, K. Masuda, R. Rautmann, and V.A. Solonikkov, eds., Springer, pp. 306–309 (1992)

6 Inviscid Vortex Propagation

Propagation of an inviscid vortex has been used as a test problem in earlier studies of finite volume methods.[8,9] The domain is two dimensional with uniform inflow $u = 1$ at $x = -0.5$, outflow conditions at $x = 3.5$, and symmetry boundary condtitions at $y = \pm 0.5$. The initial condition is a vortex in a mean flow, $(u, v) = (1 - yu_\theta, xu_\theta)$, where $u_\theta = 5r,\ 0 \le r < 0.2;\ 2 - 5r,\ 0.2 \le r < 0.4;\ 0,\ 0.4 \le r$. Two spectral element meshes are considered. The first is an 8×2 array of square elements with N=10, the second is 16×4 with N=5, for a total resolution of 81 × 21. We use the dealiased $\mathbb{P}_N - \mathbb{P}_N$ formulation (`lx2=lx1`) with viscosity $\nu = 10^{-50}$ and integrate to t=4.0, at which point the vortex has left the domain. We consider 3rd-order characteristics timestepping with Δt=.0125 and BDF3/EXT3 with Δt=.005. For each of the four cases, we consider filtered and non-filtered results with filter parameters P103=.05 for Δt=.0125 and P103=.02 for Δt=.005, giving essentially the same filter strength per unit time. For N=5 we filter the Nth mode only, whereas for for N=10 we filter both the N and N-1 modes, with the latter damped by P103/4.

Figure 5a shows the vortex structures at t=0,1,2,3 side by side for the filtered (P101=.02) case with N=5. The vortex is not Rayleigh stable and thus destabilized by any perturbation. High-resolution runs indicate that t=3 is about the limit of stability and one can see the elongation of the vortex at this time in the right-most image. Figures 5b and c show the vortex energy, which should be constant until the vortex leaves the domain. For all of the simulations, the vortex retains > 98.8% of it's initial energy to t=3. The most diffusive cases are the filtered simulations with N=5, which show a 1.1–1.2% energy loss. The N=10 cases show ∼0.5% energy loss at t=3.

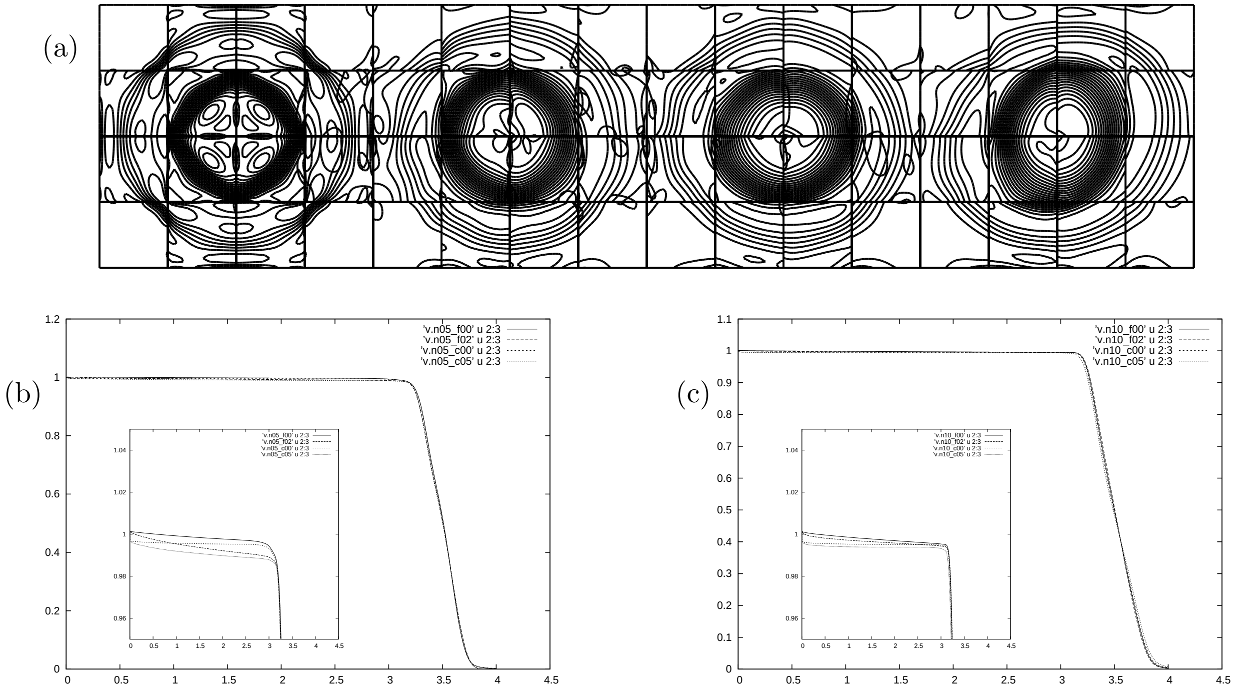

Figure 5: Propagation of an inviscid vortex: (a) contours of vorticity at t=0, 1, 2, and 3 for filtered simulation with N=5 and BDF3/EXT3, (b) energy vs time for N=5, and (c) N=10.

---

[8] P.J. O'Rourke and M.S. Sahota, "A Variable Explicit/Implicit Numerical Method for Calculating Advection on Unstructured Meshes," *J. Comp. Phys.* **143** 312–345 (1998)

[9] M.S. Sahota, P.J. O'Rourke, M.C. Cline, "Assessment of Vorticity and Angular Momentum Errors in CHAD for the Gresho Problem," Tech. Rep. LA-UR-00-2217, Theor. Fluid Dyn., Los Alamos National Laboratory, May 2000.

7 Stability of Free-Surface Channel Flow

As a check of the free-surface ALE formulation in Nek5000, we compare the growth rate for the most unstable mode for a falling film with results from linear theory.[10] For perturbation size ϵ, one can expect $O(\epsilon)$ agreement in growth rate between linear and nonlinear models.

The nominal computational domain was taken as $\Omega = [0, 2\pi] \times [-1, 0]$, tesselated with a 6×10 array of spectral elements. A uniform element distribution was used in the streamwise direction while a stretched distribution was used in the wall-normal direction. Near the wall, an element thickness of Δy=.005 was used to resolve the boundary layer of the unstable eigenmodes. The polynomial order within each element was N = 13 and BDF3/EXT3 timestepping was used with Δt=.00125. The initial conditions corresponded to the base flow plus $\epsilon := 10^{-5}$ times the most unstable eigenmode for these particular flow conditions. The domain was stretched using an affine mapping in y to accomodate the $O(\epsilon)$ surface displacement. The eigenmodes, which are defined only on y = [-1, 0], were mapped onto the nominal domain then displaced along with the mesh. The base flow was defined as $U(y) = 1 - y^2$ over the deformed mesh. The Reynolds number was Re=30000, Weber number We=0.011269332539972, and gravitational Prandtl number Pg=.00011. The applied body force was $\mathbf{f} = (2Re^{-1}, -(Re\,Pg)^{-2})$ and the surface tension was $\sigma = We$.

Mean growth rates were computed by monitoring the L^2-norm of the wall-normal velocity v and defining $\gamma(t) := t^{-1} \ln(||v(\mathbf{x}, t)||_2/||v(\mathbf{x}, 0)||_2)$. The error is defined as $e(t) := (\gamma(t) - \gamma^*)/\gamma^*$ where γ^*=0.007984943826436 is computed using linear theory. Aside from some initial transients, the error over t = [0,200] was less than .0005.

Initial tests for this problem revealed blow-up at fairly late times ($t \sim 160$). The locality and high wavenumber content in the error indicates that the blow-up is due to lack of de-aliasing in certain nonlinear terms associated with the ALE formulation. (The convective terms were dealiased; P99=3.) As illustrated in Fig. 6, such high wavenumber errors are readily addressed with low pass filtering, here implemented with P103=.05 and P101=2. We note that the error in the predicted growth rate does increase at $t > 1000$ for reasons unknown at this point, but which might be attributable to true nonlinear effects (i.e., departure from linearity).

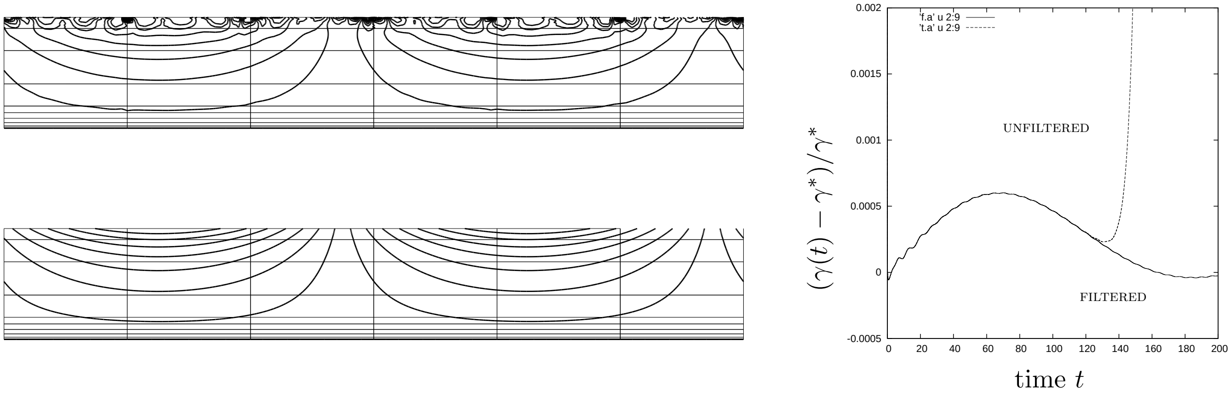

Figure 6: Eigenmodes for free-surface film flow: (left, top) contours of vertical velocity v for unfiltered and (left, bottom) filtered solution at time $t = 179.6$; (right) error in growth rate vs. t.

---

[10] Instabilities in free-surface Hartmann flow at low magnetic Prandtl numbers. Giannakis, D., Rosner, R., & Fischer, P.F. 2009, J. Fluid Mech., 636, 217-277

8 Stratified 2D Flows

This note illustrates some basic phenomena of stratified flows computed with Nek5000 using a Boussinesq approximation. We consider a two-dimensional flow with free-stream velocity U past a cylinder of diameter D and examine blocking, the Brünt-Väsäillä frequency, and the wave-like nature of stratified flow. Our discussion closely follows the introductory material given by Tritton.[11]

We assume that the density of the fluid is given by $\rho = \rho_0 + \rho'(\mathbf{x}, t)$, where the background density $\rho_0 \gg \rho'$ is constant. To first order, the perturbation ρ' only acts through the gravitational forcing in the momentum equations, given in dimensional form by

$$\rho_0 \left(\frac{\partial \mathbf{u}}{\partial t} + \mathbf{u} \cdot \nabla \mathbf{u} \right) = -\nabla p + \rho_0 \nu \nabla^2 \mathbf{u} - g \left(\rho_0 + \rho' \right) \hat{\mathbf{y}}. \tag{9}$$

The constant $-g\rho_0\hat{\mathbf{y}}$ can be absorbed into the pressure (as can any other potential field), so the dynamical influence of the stratification is driven only by the perturbation density ρ'. In addition to (9), we have the standard incompressibility constraint

$$\nabla \cdot \mathbf{u} = 0, \tag{10}$$

and the transport equation

$$\frac{\partial \rho'}{\partial t} + \mathbf{u} \cdot \nabla \rho' = \kappa \nabla^2 \rho', \tag{11}$$

which reflects the fact that the density perturbation is tied to a scalar quantity, such as salinity or temperature, that satisfies a convection-diffusion equation. (Note that Nek5000 readily handles a variable ρ_0 as well. The current studies, however, follow the formulation given by (9)–(11).)

We assume a linear profile for the initial condition of (11). That is,

$$\rho'_{y,0} := \left. \frac{\partial \rho'}{\partial y} \right|_{t=0} = constant.$$

Under these circumstances, there is an intrinsic timescale associated the stratification, which is usually expressed by its inverse, namely, the Brünt-Väsäillä frequency:

$$N_{BV} := \left(\frac{g}{\rho_0} {\rho'}_{y,0} \right)^{\frac{1}{2}}. \tag{12}$$

We return to this in the discussion below but introduce it here, prior to nondimensionalization, to stress that it is independent of any timescale associated with the external flow.

Before proceeding with the examples, we rescale the governing system of equations by the length scale D and convective timescale D/U to arrive at the nondimensional system

$$\begin{aligned} \frac{\partial \mathbf{u}}{\partial t} + \mathbf{u} \cdot \nabla \mathbf{u} &= -\nabla p + \frac{1}{Re} \nabla^2 \mathbf{u} - \frac{1}{Fr^2} (\rho' - y) \hat{\mathbf{y}} && (13) \\ \nabla \cdot \mathbf{u} &= 0 && (14) \\ \frac{\partial \rho'}{\partial t} + \mathbf{u} \cdot \nabla \rho' &= \frac{1}{Pr Re} \nabla^2 \rho'. && (15) \end{aligned}$$

Here, we have slightly abused the notation by using the same symbols for the dimensional and nondimensional variables; there will be no confusion, however, given the context in which each

---

[11] D.J. Tritton, *Physical Fluid Dynamics*, Oxford (1988).

is used. In addition to rescaling, we divided (9) and normalized the pressure by ρ_0, and have introduced three nondimensional parameters,

$$Re = \frac{UD}{\nu}, \qquad Pr = \frac{\kappa}{\nu}, \qquad Fr^{-2} = \frac{gD^2}{\rho_0 U^2} \left|\rho'_{y,0}\right|, \tag{16}$$

which are, respectively, the Reynolds number, the Prandtl (or Schmidt) number, and the Froude number. Note that the it is common to replace the Froude number by the Richardson number, $Ri := Fr^{-2}$. Finally, we have introduced an additional potential,

$$-\frac{1}{Fr^2} y\hat{\mathbf{y}}, \tag{17}$$

to remove the hydrostatic mode (associated with ρ') from the pressure.

We have computed steady-state flow past a cylinder at $Re = 10$ using the two-dimensional mesh shown in Fig. 7(a). The mesh comprises $E = 346$ elements of order $N = 7$. A uniform inflow of speed $U = 1$ is specified at the left boundary and symmetry conditions are specified on the top and bottom boundaries. The Neumann (natural) condition for the Stokes problem,

$$\frac{\partial u_i}{\partial n} + p = 0, \quad i = 1, 2,$$

is applied on the right boundary, which effectively corresponds to having $p = 0$ at the outflow. It is for this reason that we use (17) to remove the hydrostatic contribution to the pressure.

The solutions are time-marched to steady state. The initial condition for the unstratified case of Fig. 7(a) was $\mathbf{u} = (1, 0, 0)$. The converged steady-state velocity field of (a) was used as the initial condition for the stratified cases (b) and (c). the initial density profiles were $\rho' = -y$. (The cylinder is centered at $(0, 0)$.)

8.1 Steady State Results

Figures 7(b)–(d) show steady-state streamline patterns under different stratification conditions. Case (b) is standard Navier-Stokes flow without stratification. It exhibits a classic wake structure with flow separation at roughly 29 degrees from the horizontal axis and a small recirculation zone of length $\approx D/4$ aft of the cylinder.

The streamline patterns in Fig. 7(c) and (d) are in marked contrast to those in (b). In Fig. 7(c), we see that there are wakes both in front and behind the cylinder, while in (d) there is a wake only in front of the cylinder. In (c) and (d), the Froude number is $Fr = 1000^{1/2}$, which corresponds to significant stratification. This results in a phenomenon known as *blocking*, which occurs when the dynamic head of the fluid is insufficient to overcome the potential energy barrier associated with climbing above (or descending below) the cylinder. Fluid particles are essentially trapped at a given height. As explained in Tritton, the length of the forward wake is determined by viscous effects, and scales as $O(Re/Fr^2)$, provided the domain is sufficiently large.

While the flow upstream of the cylinder in Figs. 7(c) and (d) is similar in structure, the downstream behavior is decidely different. The flow conditions in (c) and (d) are identical, save that $Pr = 1$ in (c) and $Pr = 1000$ in (d). The change in the flow behavior can be explained as follows. Through density diffusion, a fluid parcel that flows close to the cylinder in case (c) takes on the local density by the time it reaches the cylinder apex. As it passes the cylinder, it has a tendency to remain at its new height and thus only slowly returns to its original height, resulting in an extended wake. For large Pr, however, the density diffusion is small. A particle passing the

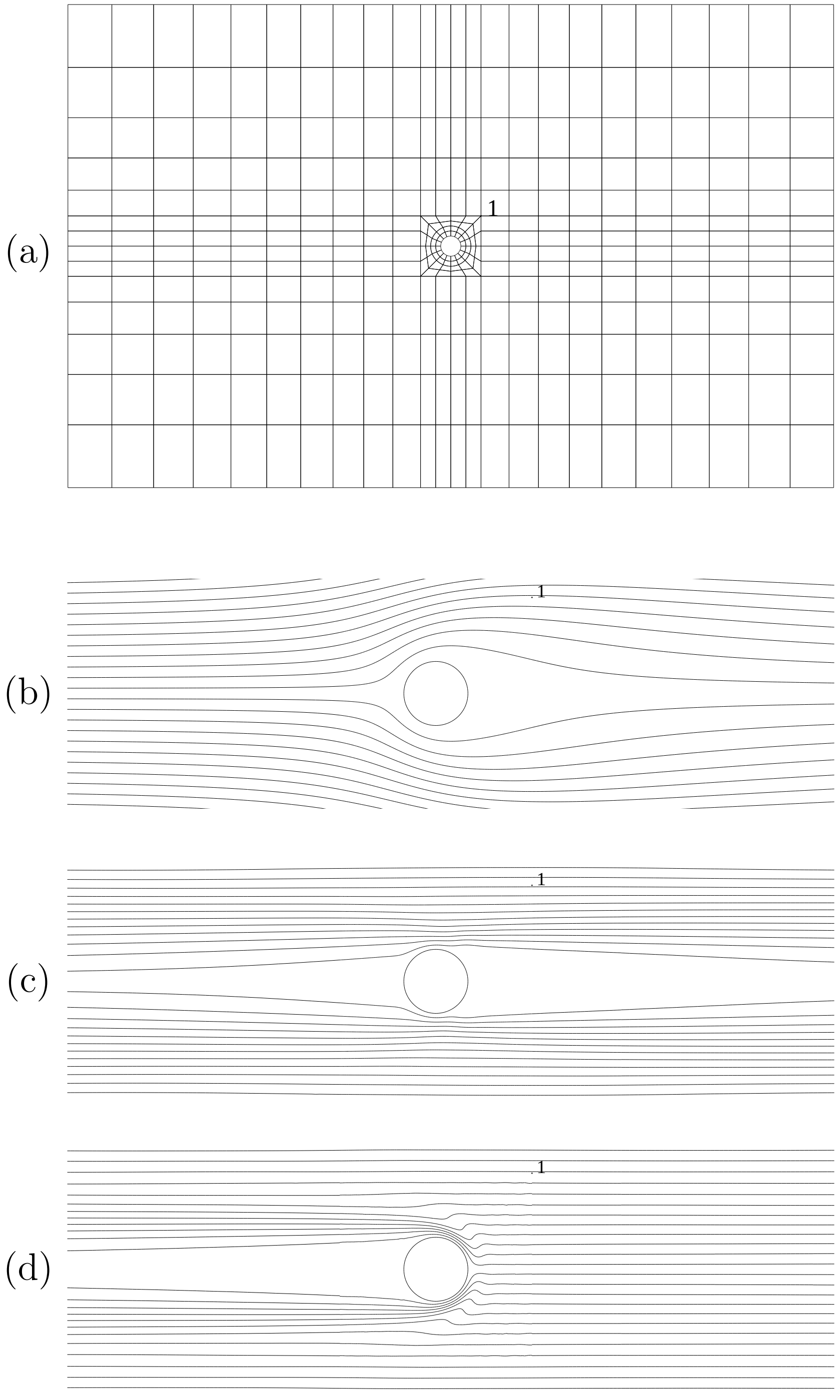

Figure 7: Examples of blocking phenomena in stratified flow at $Re = 10$: (a) spectral element mesh, (E, N)=$(384, 7)$, and steady-state streamfunction distribution for (b) no stratification, (c) Fr^{-2}=1000, $Pr = 1$, and (d) Fr^{-2}=1000, $Pr = 1000$.

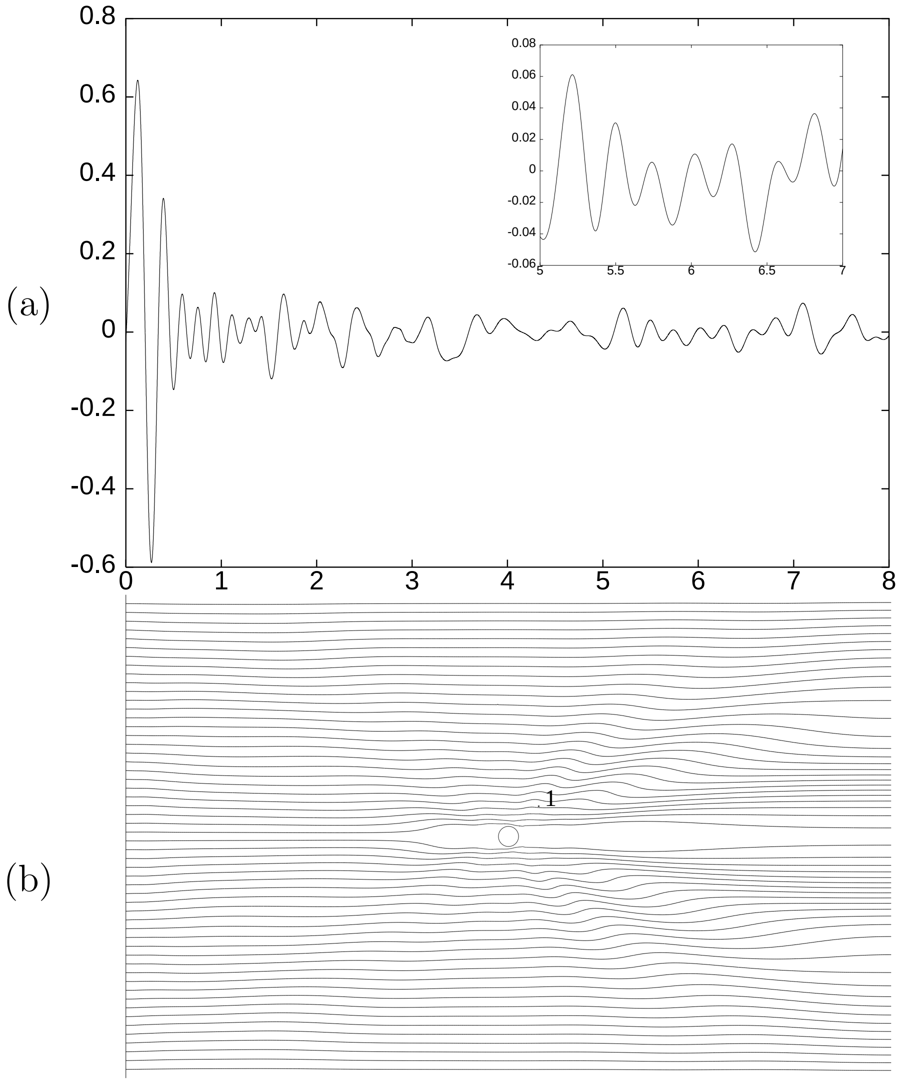

Figure 8: Wave-like response to sudden application of gravitation forcing for Fr^{-2}=1000, $Pr = 1000$: (a) time trace of v at point "1" indicated in (b); (b) instantaneous streamline pattern at $t = 0.5$.

cylinder thus retains its original density and quickly returns to its original height after passing the cylinder. This results in the streamline pattern of Fig. 7(d). (Note that the Schmidt number for salt water is $Sc \approx 700$, so $Pr = 1000$ is not far from being physically realizable.)

8.2 Unsteady Results

In addition to the steady phenomena depicted in Fig. 7, two-dimensional stratified flows exhibit interesting dynamical behavior. Under the high loading implied by a small Froude number, one can expect timescales that are significantly shorter than the convective timescale of classic incompressible flow. To illustrate, we consider the following simplified model of stratified flow. Assume that a fluid parcel with volume V is displaced a distance Δy in a body of fluid that is otherwise at rest. The restoring force is proportional to the volume of the fluid, the difference between its density and the surrounding fluid, and the gravitational constant, g. In dimensional units, we have

$$F = -V(\frac{\partial \rho}{\partial y}\Delta y)g.$$

This force accelerates the parcel in a direction opposite to Δy, resulting in the equation of motion

$$\frac{d^2 \Delta y}{dt^2} + \left(\frac{g}{\rho}\frac{\partial \rho}{\partial y}\right)\Delta y = 0,$$

which obviously leads to simple harmonic motion with frequency

$$N_{BV} := \sqrt{\frac{g}{\rho}\frac{\partial \rho}{\partial y}}.$$

Because U=1 and D=1 in the current nondimensionalization, we have from (16) $N_{BV} = Ri^{\frac{1}{2}} = Fr^{-1}$, with corresponding period $\tau_{BV} = 2\pi Fr$.

Figure 8(a) shows the history of the vertical velocity component at the point indicated by the "1" in Fig. 8(b). The initial conditions for $\mathbf{u}$ and ρ' are taken to be the steady-state flow conditions of Fig. 7(b), with Pr=1000. When the forcing is turned on, the density distribution is far from equilibrium and oscillations ensue. The oscillations in the inset in Fig. 8(a) correspond to a period of $\tau \approx 0.257$, in close agreement with $\tau_{BV} = .199$. That $\tau > \tau_{BV}$ can be understood by the fact that, because of incompressibility and the boundary conditions, the vertical displacement of any given fluid parcel must be associated with the horizontal displacement of some other parcels that add mass to the displaced system but do not add potential energy. As a consequence, the frequency will be lowered.

Tritton carries the unsteady analysis further and points out that disturbances in stably stratified flows can propagate as waves. Wave patterns are clearly evident in Fig. 8(b), which shows the instantaneous streamlines at time $t = 0.5$ for the flow associated with Fig. 8(a). Note that this convective time corresponds to the time it takes a particle in the free stream to move half a diameter. However, the wake structures and multiple waves can be seen to extend *several* diameters away from from the cylinder at this early time. We note that the loading is applied instantaneously *throughout* the domain, and that the nonequilibrium displacement of ρ' at $t = 0$ may already extend several diameters in the initial conditions.) Nonetheless, it is clear from Fig. 8(b) and other similar early-time images that information is propagating on a timescale that is much shorter than the convective timescale.

Tritton also derives a dispersion relationship for the wave phenomenon that gives the frequency as a function of the vectorial wave number

$$\omega = N_{BV} \sin\theta,$$

where θ is the angle of the wave vector with respect to the vertical axis. From the preceding estimates of τ, we can estimate the angle of the wave vector to be $\approx$ 50.6 degrees, which is in reasonable agreement with the pattern observed near history point "1" in Fig. 8(b).

8.3 Implications for Simulation

We close with a few numerical considerations encountered in these simulations.

First, because the bouyancy force is treated explicitly in Nek5000 and because it is associated with a fast timescale (for small Fr), the timestep size will generally be much less than the usual Courant-limited timestep.

Second, it is important to respect $p = 0$ at the outflow boundary, as much as possible. Also, it is important to start the simulation close to equilibrium. Otherwise, the wave motions can suck fluid in through the outflow boundary, which is usually disastrous.

Third, the wavelike nature of stratified flow implies a potential need for radiation boundary conditions, if significant wave energy is to leave the domain through an artificial domain boundary.

Fourth, we note that N_{BV} is based upon the vertical density gradient. In the case of a sharp interface, with densities ρ'_1 and ρ'_2 on either side, it should be redefined in terms of the density jump $\rho'_2 - \rho'_1$.

Fifth, turbulence, if present, will generally yield an order-unity (effective) Prandtl/Schmidt number.

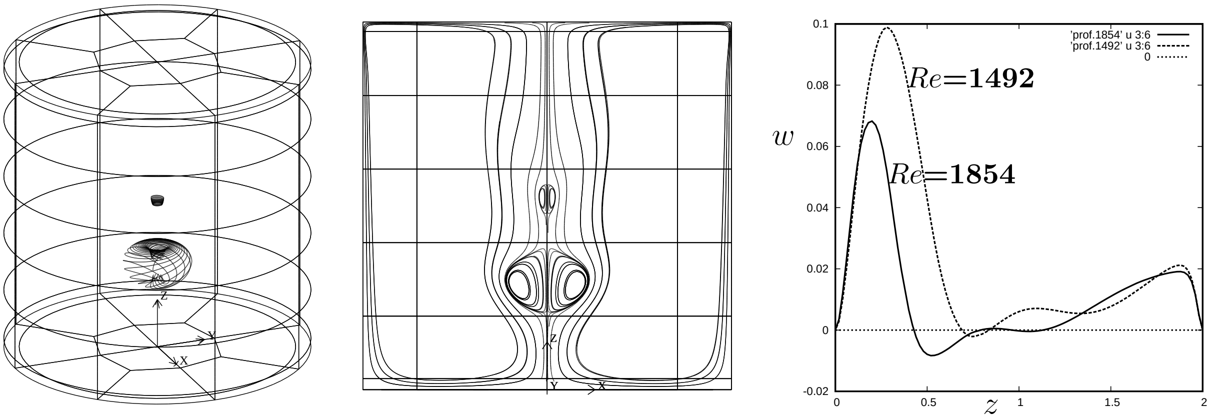

Figure 9: Vortex breakdown results: (left) streamlines for Re=1854, (center) in-plane streamlines for Re=1854, (right) vertical velocity distributions along the centerline.

9 Vortex Breakdown

Escudier[12] studied vortex breakdown in a container with a rotating lid. The domain consists of a cylindrical container of radius R and height $H = 2R$. The top lid rotates at a constant angular velocity Ω, and the Reynolds number is $Re = \Omega^2 R/\nu$. Following the standard approach, we take $\Omega = R = \rho = 1$ and set $\nu = Re^{-1}$.

The mesh in Fig. 9 is constructed from a 2D base swept through z with element boundaries at z=0, 0.06, 0.4, 0.8, 1.2, 1.6, 1.95, and 2. The mesh is concentrated near the cannister walls and near the upper and lower lids. The singularity at r=R, z=2 is handled by shearing the side walls in the top layer of elements using a 5th-order monomial. The initial and boundary condition for $z > 1.95$ are thus $(u, v) = (-y, x) * \alpha(z)$, with $\alpha = (z-2)^5/\Delta_z^5$ and $\Delta_z = .05$. The simulations are time-marched to steady state at varying spatial resolutions (N=7, 9, and 11). Simulation times of $t_f \approx 1000$ are required to form a single bubble in the $Re = 1492$ case.

Depending on the aspect ratio and Reynolds number, one can find various steady and unsteady vortex breakdown regimes with one or more "bubbles" (reversal regions) on the axis. For H/R=2, Escudier documented steady-state flows with with a single bubble at Re=1492 and two bubbles at Re=1854. The streamline plots in Fig. 9 show the bubble structures for Re=1854. Bubble locations can be inferred from zero-crossings of axial velocity w versus z at $(x, y) = (0, 0)$, shown in the right panel. These locations are tabulated below, along with experimental results of Escudier and numerical results of Sotiropoulos and Ventikos.[13]

Locations of Vertical Velocity Reversals						
	Re=1492		Re=1854			
	z_1	z_2	z_1	z_2	z_3	z_4
N=7	.689	.836	.427	.793	.960	1.131
N=9	.671	.831	.420	.776	.954	1.118
N=11	.671	.831	.420	.775	.955	1.117
Escudier	.68	.80	.42	.74	1.04(?)	1.18(?)
Sot. & Ven	.646	.774	.42	.772	.928	1.09

---

[12] M.P. Escudier, "Observations of the flow produced in a cylindrical container by a rotating endwall," *Exp. Fluids* **2** 189–196 (1984).

[13] F. Sotiropoulos & Y. Ventikos, "Transition from bubble-type vortex breakdown to columnar vortex in a confined swirling flow," *Int. J. Heat and Fluid Flow* **19** 446–458 (1998).